Chemical and Process Engineering: New Frontiers
DOI: 10.24425/cpe.2024.149463

Synthesis of $TiOF_2/CuO$ particles via coprecipitation method and their further thermal transformation to F-TiO_2/CuO

Dmitry Sofronov[a], Miroslaw Rucki[b], Alexey Lebedynskiy[c], Pavel Mateychenko[a], Sergii Minenko[d], Anna Shaposhnyk[c], Zbigniew Siemiatkowski[e], Jerzy Jozwik[f], Arkadiusz Tofil[g]

[a]Institute for Single Crystals, National Academy of Sciences of Ukraine, Prosp. Nauki, 60, Kharkiv 61178, Ukraine, e-mail 19sofonov73@gmail.com, ORCID 0000-0003-4835-7001 (D.S.); paul@isc.kharkov.ua, ORCID 0000-0002-4074-195X (P.M.);

[b]Vilnius Gediminas Technical University, Sauletekio al. 11, LT-10223 Vilnius, Lithuania; m.rucki@uthrad.pl, ORCID 0000-0001-7666-7686

[c]State Scientific Institution «Institute for Single Crystals», National Academy of Sciences of Ukraine, Prosp. Nauki, 60, Kharkiv 61178, Ukraine; alexey.lebedinsky@gmail.com, ORCID 0000-0003-2020-9939 (A.L.); annapuzan199114@gmail.com, ORCID 0000-0001-7766-4444 (A.S.);

[d]Institute for Scintillation Materials, National Academy of Sciences of Ukraine, Prosp. Nauki, 60, Kharkiv 61178, Ukraine; mss-78@ukr.net, ORCID 0000-0002-8352-1201;

[e]Faculty of Mechanical Engineering, Casimir Pulaski Radom University, Stasieckiego Str. 51, 26-600 Radom, Poland; z.siemiatkowski@uthrad.pl, ORCID 0000-0002-6830-4479;

[f]Department of Production Engineering, Mechanical Engineering Faculty, Lublin University of Technology, Nadbystrzycka 36, 20-618 Lublin, Poland; j.jozwik@pollub.pl, ORCID 0000-0002-8845-0764

[g]Institute of Technical Sciences and Aviation, The University College of Applied Sciences in Chełm, ul. Pocztowa 54, Chełm 22–100, Poland, atofil@panschelm.edu.pl, ORCID 0000-0003-2392-6597

Corresponding author: Miroslaw Rucki, e-mail: m.rucki@uthrad.pl

This article has been accepted for publication and undergone full peer review but has not been through the copyediting, typesetting, pagination and proofreading process which may lead to differences between this version and the version of record. Please cite this article as DOI: 10.24425/cpe.2024.149463.

Received: 12 April 2024 | Revised: 27 May 2024 | Accepted: 28 June 2024

Abstract. The paper presents a novel, low-cost and simple route for synthesis of $TiOF_2$/CuO and F-TiO_2/CuO out of fluoride solutions. The obtained materials after calcination can be used in various photocatalytic applications, e.g. in water treatment. It was demonstrated that control of synthesis process parameters, such as pH, allowed for synthesis of particles with different phase composition and properties. Thus, pH≤4 environment had created conditions for formation of two structures of $TiOF_2$, hexagonal and cubic ones, as well as $CuTiF_6(H_2O)_4$. Increase of Cu content promoted increase of the cubic *c*-$TiOF_2$ phase. When the solutions exhibited pH>5, the synthesized particles consisted of $(NH_4)_2TiF_6 \cdot 2H_2O$, $(NH_4)_3TiF_7$, and $(NH_4)_2CuF_4 \cdot 4H_2O$. Calcination above 300 °C provided formation of $TiOF_2$/CuO particles, while elevated temperatures of 600 °C ensured appearance of F-TiO_2/CuO material. It was found that higher copper concentrations resulted with higher fluoride percentage after calcination at 600 °C. It was also demonstrated that F-TiO_2/CuO particles synthesized at pH≤4 exhibited energy band gap *Eg* of 3.3–3.25 eV, which decreased down to 2.85 eV for higher copper(II) oxide concentrations of 10 wt.%. Notably, the particles F-TiO_2/CuO synthesized at pH>5 exhibited band gap *Eg* of 3.4–3.5 eV, which decreased down to 2.9 eV for higher CuO concentrations.

Keywords: synthesis; titanium oxyfluoride; titanium oxide; copper(II) oxide; photocatalyst

1. INTRODUCTION

Both natural and anthropogenic processes contribute to water pollution worldwide by the continuous addition of chemicals and microorganisms, as well ad domestic and industrial hazardous waste that leads to numerous health problems for humans (Balaram et al., 2023). Global water pollution is degrading people's ability to live a healthy life at an alarming rate, making necessary immediate actions to solve the problem of water scarcity and contaminations (Mittal et al., 2023). Aquatic environment contains a variety of contaminants like endocrine disrupting compounds, polycyclic aromatic hydrocarbons, pesticides, polychlorinated biphenyl, phenols and carboxylic acids, pharmaceuticals, and industrial chemicals (Rueda-Marquez et al., 2020; Poblete et al., 2020; Miklos et al. 2018). The application of low-cost materials to deal with environmental pollution has been addressed for years, and the scientific interest seems currently to be increasing (Núñez-Delgado et al., 2023). At present, the heterogeneous catalysis, especially using TiO_2-based photocatalytic membrane reactors, is among the most important water treatment methods due to its high efficiency to degrade both organic and inorganic pollutants (Riaz and Park, 2020; Tatarchuk et al., 2018; Garg et al., 2019; Szczepanik, 2017).

Titanium oxide TiO_2 is a semiconductor suitable for photocatalysis and solar energy conversion due to its properties, such as stability against photo- and chemical corrosion, low cost, as well as high cleaning and antibacterial effects (Janczarek et al., 2022; Edelmannová et al., 2018; Ibrahim et al., 2020). The value of the band gap differs for different phases, namely for anatase $Eg = 3.2$ eV, for rutile $Eg = 3.0$ eV and for brookite $Eg = 3.4$ eV (Edelmannová et al., 2018). However, the inherent limitations and high operating costs limit the practical applications of TiO_2 photocatalytic membranes, which motivates researchers to search for new approaches to enhancing their photocatalytic performance, including metal and non-metal doping, control over reaction conditions, fabrication of heterojunction structures, increase in hydrophilicity, and increase in membrane porosity (Wang, Chen et al., 2022).

One of the most popular directions for improving the photocatalytic properties of titanium oxide particles is the creation of TiO_2-based heterostructural catalysts. They achieve a more efficient separation of charge carriers due to the p-n transition, which leads to an increase in the quantum efficiency of the catalyst (Liang et al. 2022). Moreover, the additional deposition of semiconductor particles active in the visible range of the solar spectrum contributes to the expansion of the absorption spectrum of the photocatalyst. There are many proposition published on usage of noble metals to create this sort of heterostructures, among them Ag (Cotolan et al., 2016), Au (Ayati et al. 2014), Pt (Gupta et al., 2016), but also oxides Ag_2O

(Gao and Wang, 2021), CuO (Abdalamir et al., 2022), Fe_2O_3 (Mohamed et al., 2020), V_2O_5 (Kayani et al., 2021), Co_2O_3 (Jacob et al., 2022), etc., phosphates (Amaral et al., 2022) or sulfides (Moridon et al., 2022).

There are also reports on surface fluorination effects on the photocatalytic reactivities through the action of surface ⋮ Ti−F group as an electron-trapping site, reducing interfacial electron transfer rates (Park and Choi, 2004; Li et al., 2005; Dozzi et al., 2013). Guo et al. (2023) demonstrated that the NO oxidation efficiency of F-TiO_2 particles could be higher by more than 40% compared to that of TiO_2. Among methods of F-TiO_2 synthesis, sol-gel method was proposed (Li et al., 2007), but also spray pyrolysis (Todorova et al., 2008), or thermal decomposition (Sofronov et al., 2022). Precursor for F-TiO_2 synthesis is titanium oxyfluoride $TiOF_2$, which can be used itself as a photocatalyst (Shian and Sandhage, 2010; Wang et al., 2014). In the present study, we focused on coprecipitation methodology, when both the main component and a modifier can be precipitated out of the single solution simultaneously, forming a system made up from several phases. In particular, the work is dedicated to the process of precipitation of particular components and how the target product can be obtained.

Synthesis via coprecipitation is one of the mostly quoted processes in the literature, spotlighted as a simple, cost-effective and time-saving and eco-friendly route, easily transposable on an industrial application scale (Cruz et al., 2018). Microemulsion coprecipitation belongs to a bottom-up approach for the metal oxide nanomaterial synthesis, where control of such parameters as pH, concentration of solution, viscosity, temperature, surface tension, and stirring speed provide the desirable properties of the product (Siva Prasanna et al., 2019).

In the typical coprecipitation reaction, two or more water-soluble salts are used, and advantage is taken of different solubility of these salts in water. During the reaction, one or more water-insoluble salts are formed in the liquid phase, so that precipitation takes place, but not by just dropping out in the solution. The newly formed ions establish the shell precipitating on the core surfaces (Dembski et al., 2018).

Titanium oxyfluoride can be synthesized through hydrolysis of aqueous solution, which is easy and convenient route of high practical importance. During synthesis, additional dopants can be introduced to form heterostructures of desired properties. In our research, copper(II) oxide CuO was chosen as the dopant. Copper(II) oxide has recently attracted research interest in the area of photocatalyst formation with heterojunction structures due to its availability, good stability and its absorption in visible light spectrum. CuO is a typical p-type

semiconducting compound with a monoclinic structure and a low band gap of Eg = 1.2–2.0 eV. Since Eg lays between the wide band gap of TiO_2, it is possible to form p–n junctions of CuO with n-type TiO_2 (Chaudhari and Mishra, 2016). CuO has been demonstrated to be suitable for a wide range of potential technological applications such as gas sensors, biosensors, superconductors, photovoltaic, photocatalytic systems. In particular, inserting CuO into the structure of $TiOF_2$ can cause an increase in photocatalytic activity, because it creates an internal electric field, which promotes electron-hole separation and decelerates the charge carrier recombination (Chowdhury et al., 2017; Banas-Gac et al., 2023). It was found that CuO/TiO_2–F composite exhibited 2.2 higher rate of hydroxyl radical generation than that for TiO_2–F (Castañeda et al., 2022). Since there are not many reports on CuO/TiO_2–F composites (Lathe and Palve, 2023), this research direction seems to be novel and promising due to advantages of both F-TiO_2 particles and CuO addition.

The present research is a continuation of the investigations reported previously (D.S. Sofronov et al., 2023) on the simple and fast synthesis of $TiOF_2$ particles out of fluoride solution. It was found that in the hydrolysis process, two polymorphous modifications of titanium oxyfluoride were formed, cubic structure with spatial group ($Pm\bar{3}m$) and hexagonal one with group ($R\bar{3}c$). What was the most important, the correlation between proportion of the two structures in the synthesized powder and the synthesis process conditions was determined. Undoubtedly, fabrication of the doped $TiOF_2$–based particles with the desired properties is of high scientific and practical interest.

Thus, this work was focused on the synthesis of $TiOF_2$/CuO particles via a similar route of precipitation out of fluoride solutions. First of all, it was aimed at determination of the synthesis conditions effect on the structure and morphology of the as-obtained particles, which was the main determinant of the properties of the powder. Moreover, considering one of the applications of the titanium oxyfluoride, the process of its thermal transformation into F-TiO_2/CuO was investigated, too. Based on the collected data, it was assumed that hydrolysis of aqueous solution can be an effective low-cost coprecipitation route for F-TiO_2/CuO synthesis.

2. MATERIALS AND METHODS

2.1 Test campaign

Keeping in mind the main purpose of the research, various conditions of the synthesis process were tested, and the relevant characteristics of the obtained particles were measured. In particular:

- precipitation process was carried out in different environments, at pH 6 and higher, representing neutral and alkaline environments, and at pH 1 providing acid environment,
- $TiOF_2$ powder was doped with copper ions in proportions of 0.5%, 1%, 2%, 5%, and 10%,

Further analysis of phase composition was different, since the environment of synthesis resulted with different phases in the synthesized powders. In particular, percentage of cubic and hexagonal $TiOF_2$ was measured for acid conditions, and appearance of $CuTiF_6(H_2O)_4$ was analyzed, while $(NH_4)_2TiF_6(H_2O)_2$, $(NH_4)_3TiF_7$, and $(NH_4)_2CuF_4(H_2O)_2$ were analyzed for pH 6 and higher.

Next, the following experiments and measurements were performed:

- calcination was carried out in temperatures of 300°C, 400°C, 500°C, and 600°C and the phase composition was compared to that obtained in the room temperature (RT),
- analysis of infrared spectra, elemental composition, morphology and particle sizes was performed for the powders before and after calcination,
- decomposition reactions were described,

Initial test of the optical properties was made and the band gap energy of the tested substances was assessed.

2.2 Reagents

The main source of titanium was the product marked BT1-00, which according to international standard GOST 19807-91 contained maximum amount of additions as follows: 0.08 wt.% of Si, 0.15 wt.% of Fe, 0.10 wt.% of oxygen, 0.008 wt.% of hydrogen, 0.04 wt.% of nitrogen, 0.05 wt.% of carbon, and sum of other elements 0.10 wt.%. Also were used hydrofluoric acid HF 45.1%, nitric acid 56% (1.35 g/cm^3), and trihydrate copper(II) nitrate ($Cu(NO_3)_2{\cdot}3H_2O$), all delivered by Reachem company (Russia). The substances were chemically pure, and to prepare solutions, the distillated water was used.

It should be noted that environmental impact and health hazards of HF were minimized during synthesis. After the process was completed, no hydrofluoric acid was left either in the

solutions or in the synthesized powders, which also underwent thermal treatment. The used up solutions were utilized according to the standard procedures.

2.3 Synthesis procedure

Metallic titanium in the amount of 2 g was placed for dissolution in a fluoroplastic vessel. It was fully dissolved in 10 mL of distilled water and 10 mL of hydrofluoric acid. Then, a few drops of the concentrated nitric acid were added to make the solution colorless. After that, adding the certain amount of distillated water, the overall volume was increased up to 50 mL. Next, the respective weighed portions of copper nitrate were added to obtain desired concentrations of 0.5, 1, 2, 5, and 10 wt.%, as calculated in relation to CuO. As-prepared solution was heated up to boiling temperature and boiled for 30 minutes, or up to 4 hours. Due to evaporation, the precursor in form of a dry powder appeared, which was then subject to calcination at temperatures 300 °C, 400 °C, 500 °C, and 600 °C in air for 1 hour. Dependent on the copper content, the as-obtained powders had colors from white to dark grey.

2.4 Equipment

In order to gain information on the decomposition process of doped titanium oxyfluoride particles, and to compare it with that of non-doped ones, the infrared spectra were found useful. The analysis of IR spectra was performed with Spectrum One FT-IR Spectrometer with KBr tablets. The device was made by PerkinElmer (USA). The spectra from the range between 400 and 4000 cm^{-1} were registered at room temperature. Phase compositions of the powders were analyzed using the X-ray diffractometry (XRD) device with a graphite monochromator and Cu Kα radiation of wavelength λ=1.54187Å. The phase identification was performed both in qualitative and quantitative terms, using Profex program (Döbelin and Kleeberg, 2015). The presence of particular chemical compounds has been confirmed through a comparison between experimental XRD patterns and reference ones using a routine procedure performed automatically by Profex software. For this work, reference XRD patterns were taken from the Crystallography Open Database.

Shimadzu UV-2450 spectrophotometer with $BaSO_4$ reference allowed for collection of UV–vis diffuse reflectance records in the range of 200–900 nm. The band gap energy (*Eg*) of aerogel photocatalysts was determined by plotting $h\nu(eV)*F(R_{oo}))^{1/2}$ as a function of the energy hν(eV) with $F(R) = (1-R)^2/2R$, where R is the reflectance. The extrapolation of the linear parts of $h\nu(eV)*F(R_{oo}))^{1/2}$ with the abscissa axis allowed the calculation of the gap

energy *Eg*. The morphology and elemental composition of the samples were studied using scanning electron microscope JSM-6390LV and AZtecEnergy X-maxN50 energy-dispersive spectrometer.

3. RESULTS AND DISCUSSION

During the experiments it was found that dependent on pH of synthesis environment, the powder precipitated out of fluoride solutions had different phase composition. The analysis showed that the differentiation took place at pH values between 5 and 6. Thus, acid environment of pH 4 and lower, provided similar phase composition of the samples, and similar pattern of their thermal transformation. In turn, at pH 6 and higher, other phase composition and thermal transformation pattern was observed. For this reason, analysis of the results is convenient to be divided into two respective subsections, corresponding with two groups of the similar phase compositions, describing particles precipitation in acid environment and separately precipitation in neutral and alkaline environments. The respective results of phase composition, electron microscopy and IR spectrometry of the synthesized particles and their subsequent thermal transformation to F-TiO_2/CuO are presented in the following subsections, respectively.

3.1 Particle precipitation in acid environment

After evaporation, white precipitate was formed from the titanium fluoride solution with pH 1. Bluish tint appeared, when the copper content in the samples was more than 2 wt.%. Diffractograms of the precursor samples with different copper concentrations are shown in Figure 1. Table 1 contains the data from X-ray diffraction analysis for the same samples, demonstrating the effect of copper concentration in the precursor on the phase composition of the samples.

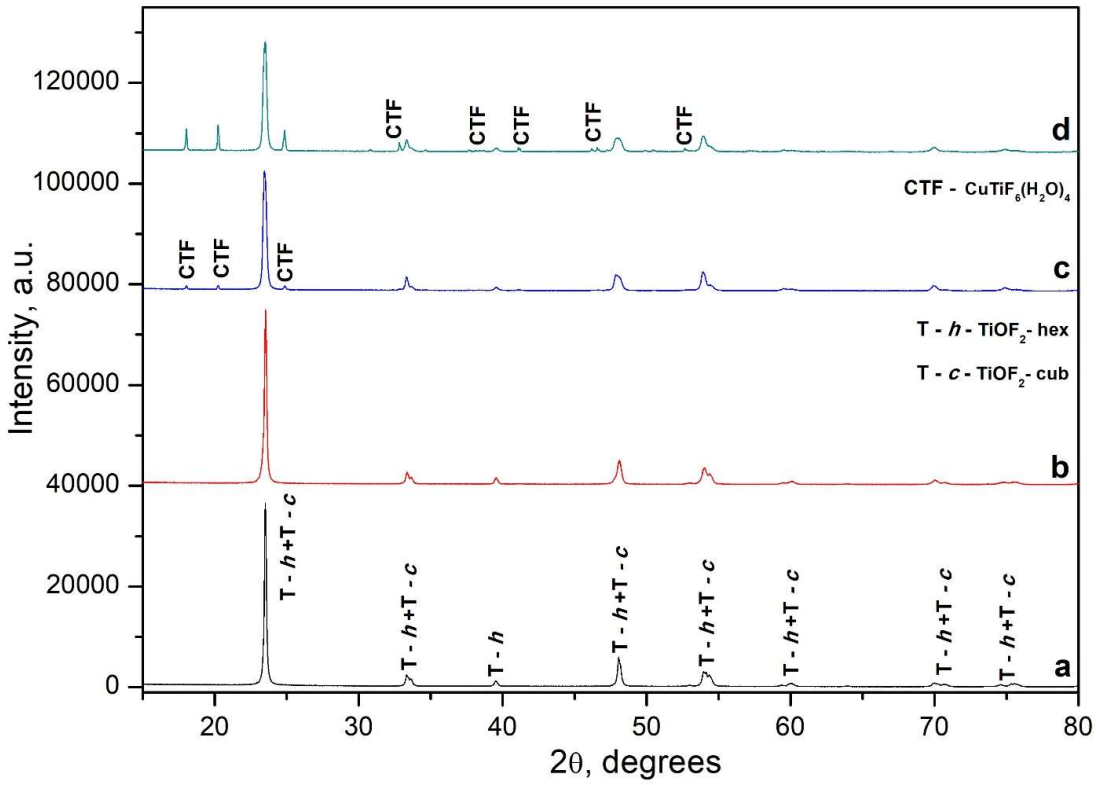

Figure 1. XRD diagrams of the particles synthesized at pH 1. Respective copper content in the samples was 1 wt.% (curve a), 2 wt.% (b), 5 wt.% (c), and 10 wt.% (d) (calculated in relation to CuO).

Table 1. Phase composition of $TiOF_2$ powder doped with copper ions.

Copper content, wt.%	Phase composition		
	c-$TiOF_2$, %	*h*-$TiOF_2$, %	$CuTiF_6(H_2O)_4$, %
1	8	92	-
2	27	73	-
5	42	54	4
10	28	50	22

The obtained results demonstrated that addition of copper 1 wt.% and 2 wt.%, as calculated in relation to CuO, contributed to the synthesis of a single phase $TiOF_2$ precipitates. On the other

hand, the samples synthesized with 5 wt.%, as calculated in relation to CuO, consisted of two phases, namely, titanium oxyfluoride and copper fluorotitanate tetrahydrate ($CuTiF_6(H_2O)_4$. Further increase of the copper proportion up to 10 wt.%, as calculated in relation to CuO, had effect in increase of the copper fluorotitanate tetrahydrate from 4% up to 22% in the resulting sample.

It should be noted that increase of the copper proportion in the precursor has also impact on the ratio between the cubic (*c*-$TiOF_2$) (marked as T-C in Fig. 1) and hexagonal (*h*-$TiOF_2$) (marked as T-h in Fig. 1) phases of titanium oxyfluoride, with the amount of hexagonal structure being decreased (see Table 1). Thus, it can be assumed that the addition of copper ions contributed to the formation of *c*-$TiOF_2$ phase. Noteworthy, neither pH increase up to 4, nor addition of the hydrofluoric acid during synthesis had any effect on the phase composition or on the morphological features of the obtained powder. IR spectra of the synthesized precursors are shown in Figure 2.

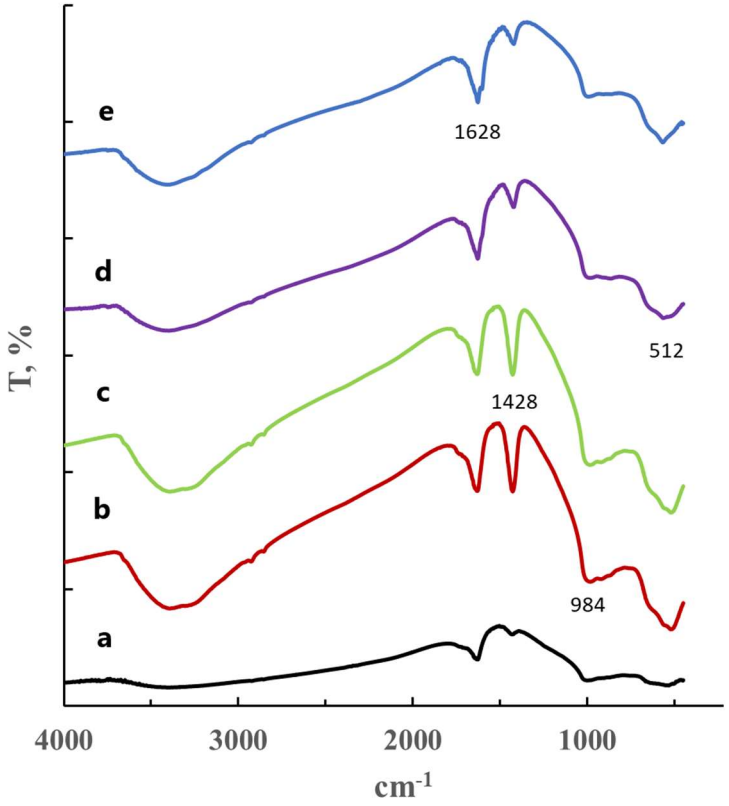

Figure 2. IR spectra of the particles synthesized at pH 1 with copper content of 0.5 wt.% (curve a), 1 wt.% (b), 2 wt.% (c), 5 wt.% (d), and 10 wt.% (e) (calculated in relation to CuO).

Figure 2 demonstrates that in the spectrum of $TiOF_2$ doped with 5 wt.% of Cu (calculated in relation to CuO), the absorption band appeared with maximum at 1628 cm^{-1} related to the deformation vibrations of the water molecules adsorbed on the tested particles surfaces. Other

absorption bands can be seen at 984 cm^{-1} and 512 cm^{-1}, attributed to the Ti–O–F and Ti–O bond vibrations, respectively. However, regardless of the copper content, no absorption band was distinguished that would prove the presence of $CuTiF_6(H_2O)_4$. Perhaps, it was not distinguishable because the absorption band of TiF_6^{2-} ion in the area of 500–600 cm^{-1} overlapped with the one belonging to Ti–O–F ion of the titanium oxyfluoride in the area of 500–1300 cm^{-1}. It can be found in literature that the presence of $ZnTiF_6 \cdot 6H_2O$ and $MnTiF_6 \cdot 6H_2O$ corresponded with the respective bands of 530 cm^{-1} and 545 cm^{-1} (Choudhury et al., 1983).

Figure 3 presents the SEM images of the synthesized particles. When copper was present in the concentration of 0.5 wt.%, agglomerated particles were formed of spherical form with diameters up to 1 μm. When the proportion of the copper increased, the particles grew larger, up to 2–3 μm, as seen in Figures 3b–d. Moreover, the form of the particles differentiated.

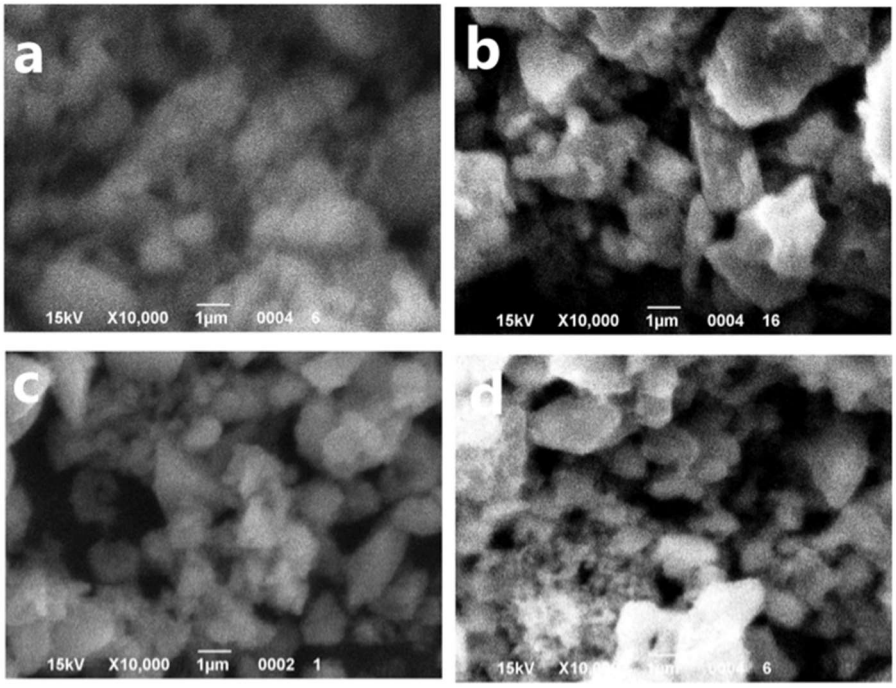

Figure 3. SEM images of the particles synthesized at pH 1 with copper addition of 0.5 wt.% (a), 1 wt.% (b), 5 wt.% (c), and 10 wt.% (d) (calculated in relation to CuO).

In order to form a CuO phase, calcination procedure of the initial precursor was performed in air for 1 hour, applying different temperatures. Figure 4 presents the diffractograms obtained for the powders calcined at different temperatures from 300 °C up to 600 °C. Results of the quantitative phase analysis of the same samples are collected in Table 2.

Table 2. Changes in the phase composition of the precursor with 10 wt.% of copper (calculated in relation to CuO), dependent on the calcination temperature.

T, °C	*h*-$TiOF_2$, %	*c*-$TiOF_2$, %	$CuTiF_6(H_2O)_4$, %	Anatase, %	Rutile, %	CuO, %
RT	51.3	26.3	22.43	-	-	-
300	63.1	7.9	9.42	17.2	2.38	-
400	17.06	6.8	2	57.32	14.76	2.6
500	14.86	3.91	-	29	49.37	2.83
600	-	-	-	16.04	77.55	8.41

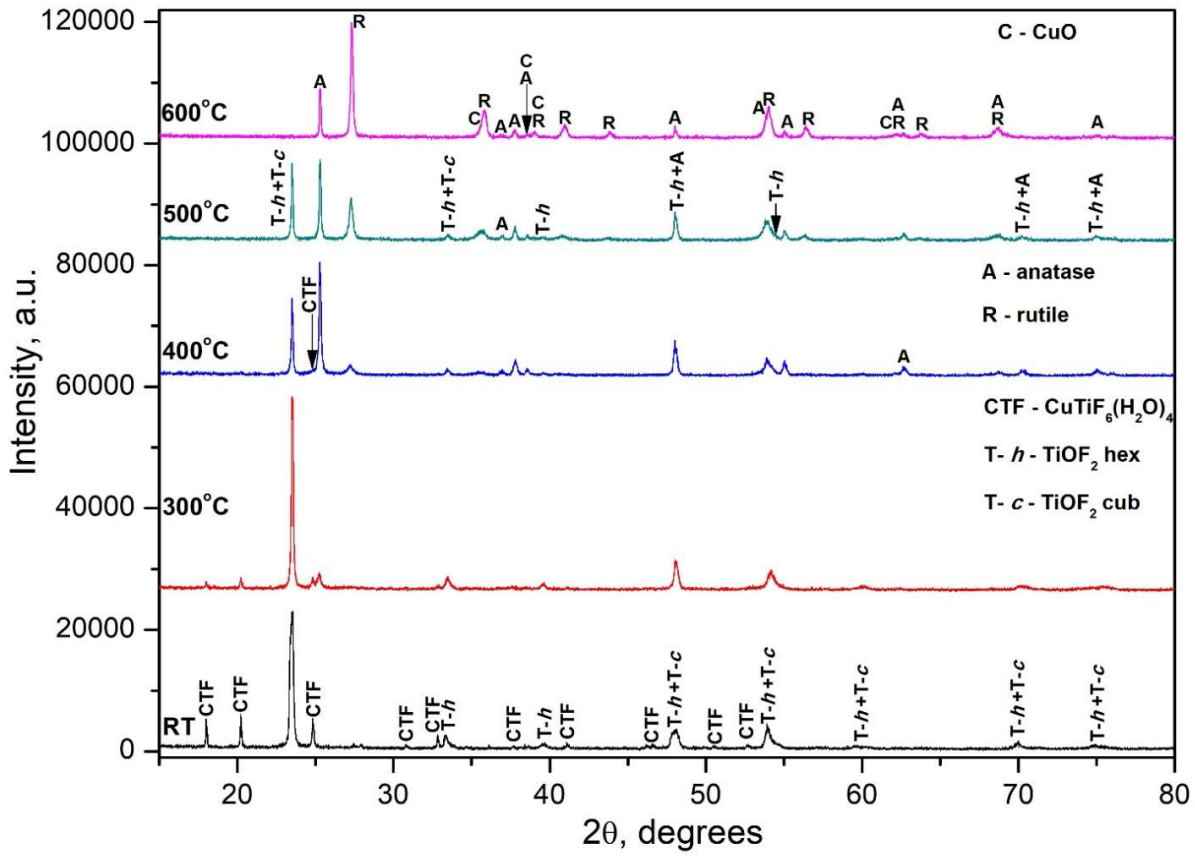

Figure 4. XRD diagrams of the particles synthesized at pH 1 with copper addition of 0.5 wt.% (a), 1 wt.% (b), 5 wt.% (c), and 10 wt.% (d) (calculated in relation to CuO).

The XRD analysis demonstrated that the phase of CuO started to form at calcination temperatures above 300 °C. In the diffractograms, when the reflexes related to the presence of CuO appeared, at the same time disappeared the ones corresponding with $CuTiF_6(H_2O)_4$. That led to a conclusion that CuO phase is mainly formed out of $CuTiF_6(H_2O)_4$. Calcination process at temperature T_c = 300 °C resulted with appearance of anatase and rutile phases in

the titanium dioxide sample. Further increase of the calcination temperatures was accompanied by the increase of the rutile content. Rutile formation during the synthesis of copper-doped TiO_2 particles was reported previously in the literature (Lin and Yang, 2014). Moreover, Wang et al. (2022) paid attention to the intensification of the reflexes from the rutile phase of TiO_2 after increase of the CuO proportion in the samples. These papers discussed in detail why the titanium dioxide is formed in these two polymorph structures after addition of the copper dopant. In should be emphasized that the obtained data allowed for the conclusion, that the main phase of titanium oxyfluoride was fully transformed to the titanium dioxide after calcination at temperatures above 600 °C. Figure 5 presents the IR spectra of the calcined particles.

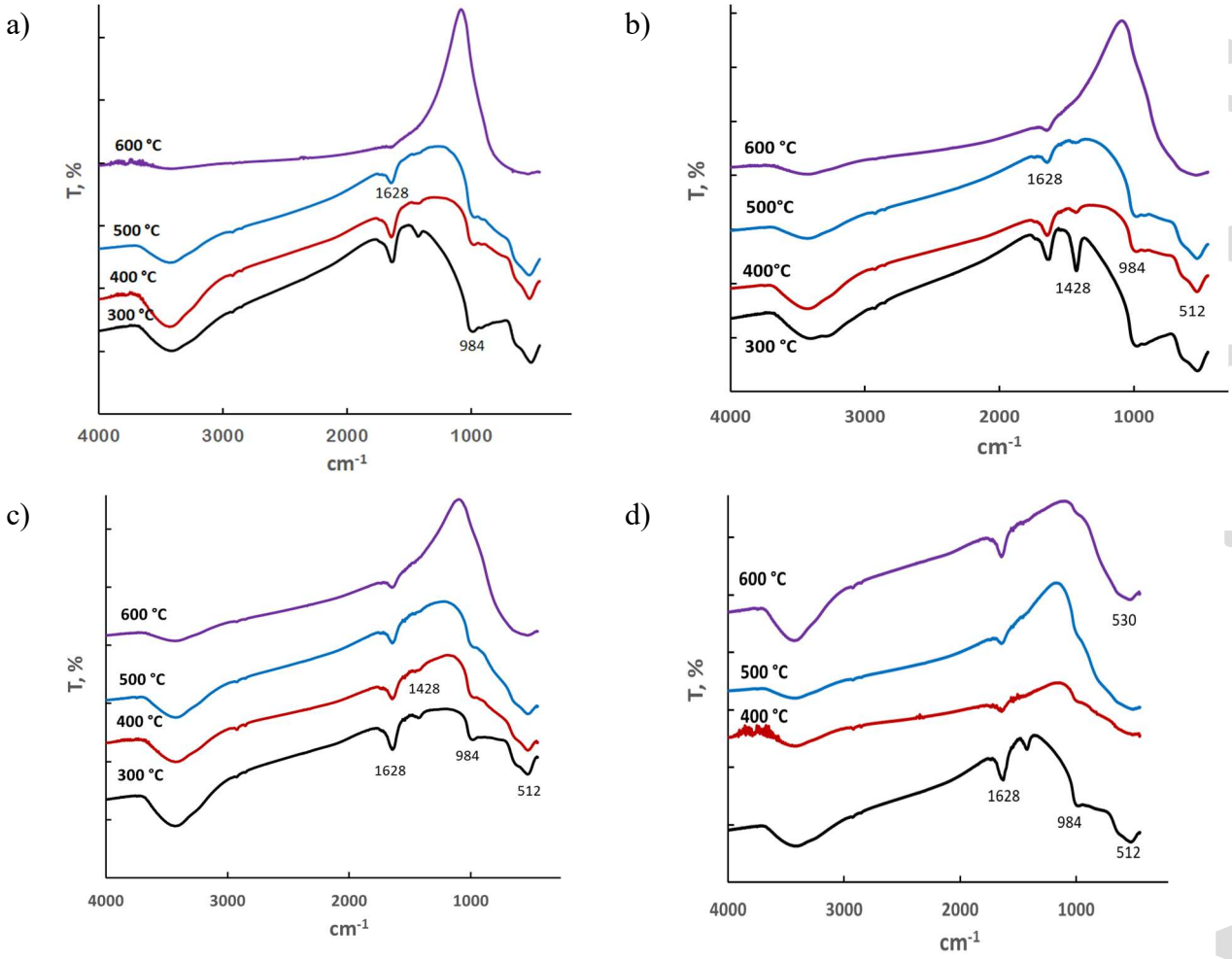

Figure 5. The IR spectra of the particles synthesized at pH 1 and calcined for 1 hour at different temperatures with different proportion of copper (calculated in relation to CuO): a) 0.5 wt.%, b) 1 wt.%, c) 5 wt.%, and d) 10 wt.%.

Direct impact of CuO was not found, since no absorption band corresponding with copper compounds was registered. Irrespective on the copper content, absorption bands were noted at 984 cm^{-1} and 512 cm^{-1}, corresponding to the vibrations of Ti–O–F and Ti–O bonds, respectively. Increase of calcination temperature up to 400 °C caused decrease of the absorption band intensity at 984 cm^{-1}. This phenomenon proved decomposition of the titanium oxyfluoride and dependence of titania formation on the copper content. In particular, for the samples calcined at 600 °C, IR spectra corresponded with those of titanium dioxide. At the same time, when CuO concentration was 10 wt.%, the absorption band at 984 cm^{-1} practically disappeared from the IR spectrum of the sample calcined at 500 °C. In other words, the vibrations of Ti–O–F bonds were not registered for these samples.

Figures 6 and 7 demonstrate that formation of new phases of titanium dioxide and copper(II) oxide was accompanied by the decrease of the powder particle dimensions. At low concentrations of copper up to 1 wt.%, particle size did not change substantially, as seen in Fig. 6. However, high content of copper (10 wt.%) caused formation of fine-dispersed powder with spherical particles as seen in Fig. 7.

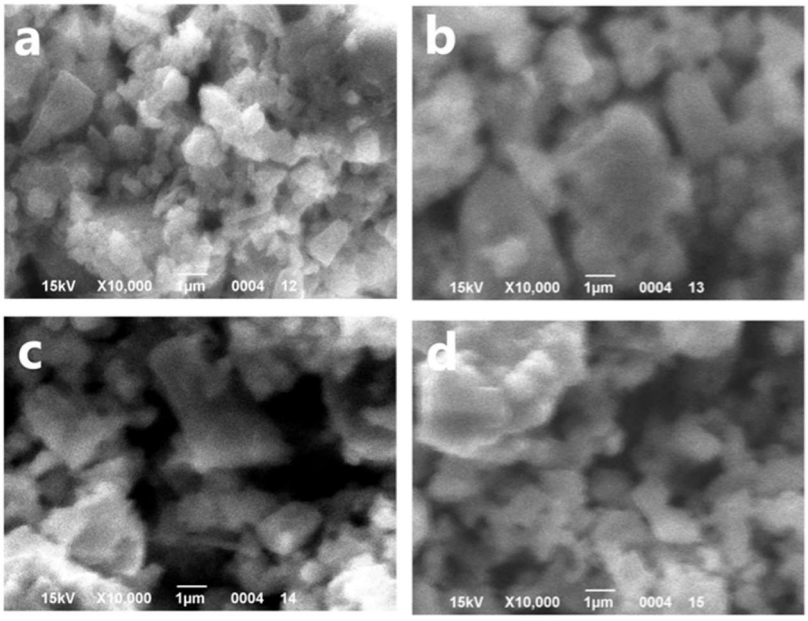

Figure 6. SEM images of the particles with 1 wt.% of copper after calcination at different temperatures: a) 300 °C, b) 400 °C, c) 500 °C, d) 600 °C.

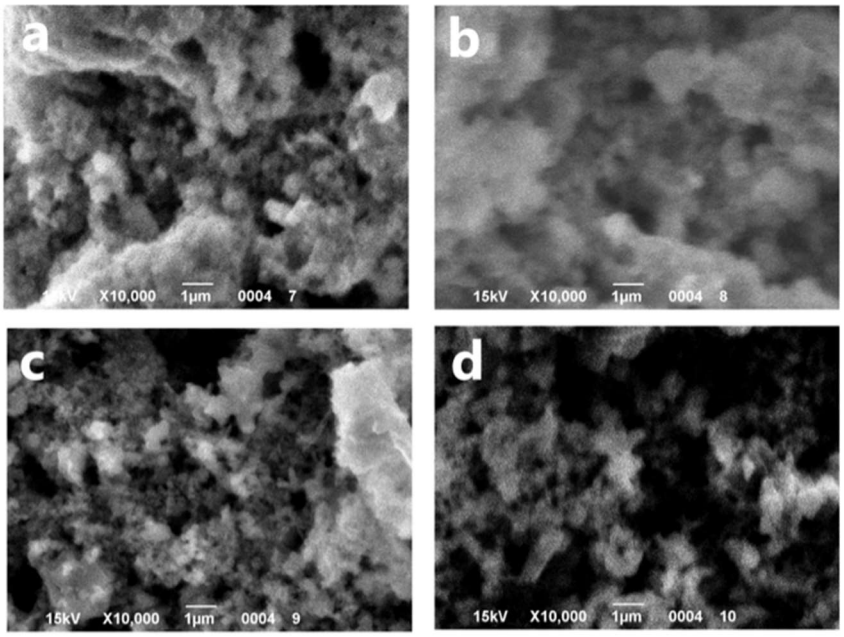

Figure 7. SEM images of the particles with 10 wt.% of copper calculated in relation to CuO, after calcination at different temperatures: a) 300 °C, b) 400 °C, c) 500 °C, d) 600 °C.

The results of elemental analysis collected in Tab. 3 confirmed that decomposition of the titanium oxyfluoride took place at temperatures higher than 300 °C. In this temperature range, significant decrease of fluorine was noted with the increase of oxygen in the samples.

Table 3. Results of elemental analysis of the particles synthesized at pH 1.

Calcination temperature, °C	Element, wt.%			
	Ti	O	F	Cu
0.5 wt.% of CuO				
RT	32.6	15.2	52.1	0.1
300	35.6	15.4	48.9	0.1
400	41.2	20.1	38.5	0.2
500	43.6	23.0	33.1	0.3
600	58.2	39.1	2.3	0.4
1 wt.% of CuO				
RT	31.0	16.6	52.0	0.4
300	34.5	15.6	49.5	0.4
400	40.4	20.9	38.0	0.7
500	44.4	20.9	33.8	0.9

600	57.0	39.1	2.9	1.0
2 wt.% of CuO				
RT	33.2	15.7	50.6	0.5
300	38.5	17.4	43.5	0.6
400	40.0	34.8	35.0	1.2
500	44.3	30.2	23.0	2.5
600	51.0	42.3	3.6	3.1
5 wt.% of CuO				
RT	33.4	16.2	48.5	1.9
300	33.8	20.7	42.4	3.1
400	42.1	20.6	33.8	3.5
500	43.3	25.8	25.5	5.4
600	48.0	37.1	7.3	7.6
10 wt.% of CuO				
RT	34.6	12.5	47	5
300	35.6	22	36	5.2
400	42.8	33	18	8.6
500	42.7	28	19.9	8.7
600	42	37.3	9.9	9.9

This phenomenon proved formation of titanium dioxide. At the same time, fluorine was found in the samples calcined at 600 °C with no traces of presence of titanium oxufluoride in XRD data. This can be attributed to the formation of fluorinated titanium dioxide F-TiO_2 (Dozzi et al., 2013; Shian and Sandhage, 2010). Notably, the fluorine content in titanium dioxide increased with the increase of copper concentration in the samples.

Thus, precipitation process in acid environment (pH < 4) led to formation of a powder consisting of cubic and tetragonal $TiOF_2$, and $CuTiF_6 \cdot 4H_2O$ phase. Heating caused decomposition, dehydration and hydrolysis according to the following pattern:

$$CuTiF_6 + 2H_2O \rightarrow CuO + TiOF_2 + 4HF \quad (1)$$

In fact, copper hexafluorotitanate decomposition was fully completed at 400 °C. In the interval between 300 °C and 400 °C, decomposition of titanium oxyfluoride started according to the following reaction:

$$TiOF_2 + H_2O \rightarrow TiO_2 + HF \quad (2)$$

It was completed at 600 °C with formation of fluorinated titanium dioxide in rutile and anatase phases. Notably, proportion of the resulting TiO_2 phases is dependent on the copper concentration. Increase of the copper content caused increase of the rutile phase and decrease of the full decomposition temperature of titanium oxyfluoride.

3.2 Precipitation of the particles in neutral and alkaline environments

It should be noted that the obtained results were identical for both neutral and alkaline environments, i.e. for pH 6 and higher. Increase of precipitation environment pH up to 8 or 9.5 did not result in different phase composition. In all the cases, XRD diagrams were similar to that shown in Fig. 8a revealing reflexes ascribed to ammonium fluorotitanate and fluorocuprate. In the entire range of pH values from 6 up to 9.5, both phase composition and subsequent thermal transformation pattern were similar, the results for pH6 presented below can be fully representative for the entire group.

XRD analysis of the powder synthesized at pH 6 demonstrated that right after synthesis, the samples represented a multiphase composition. The following compounds were identified: $(NH_4)_2TiF_6(H_2O)_2$, $(NH_4)_3TiF_7$ и $(NH_4)_2CuF_4(H_2O)_2$. Apart from those, also other phases were present, which can be seen from the XRD diagrams in Fig. 8. Moreover, an amorphous component was present, too.

When the samples underwent heating up to 300 °C, decomposition of the ($(NH_4)_2TiF_6(H_2O)_2$, $(NH_4)_3TiF_7$, and $(NH_4)_2CuF_4(H_2O)_2$ compounds took place, accompanied by formation of new $TiOF_2$ and $CuTiF_6(H_2O)_4$. For that case, diffractograms contained some reflexes from unidentified phases. Noteworthy, after synthesis from acid solution and calcination at this temperature, presence of titanium dioxide was observed.

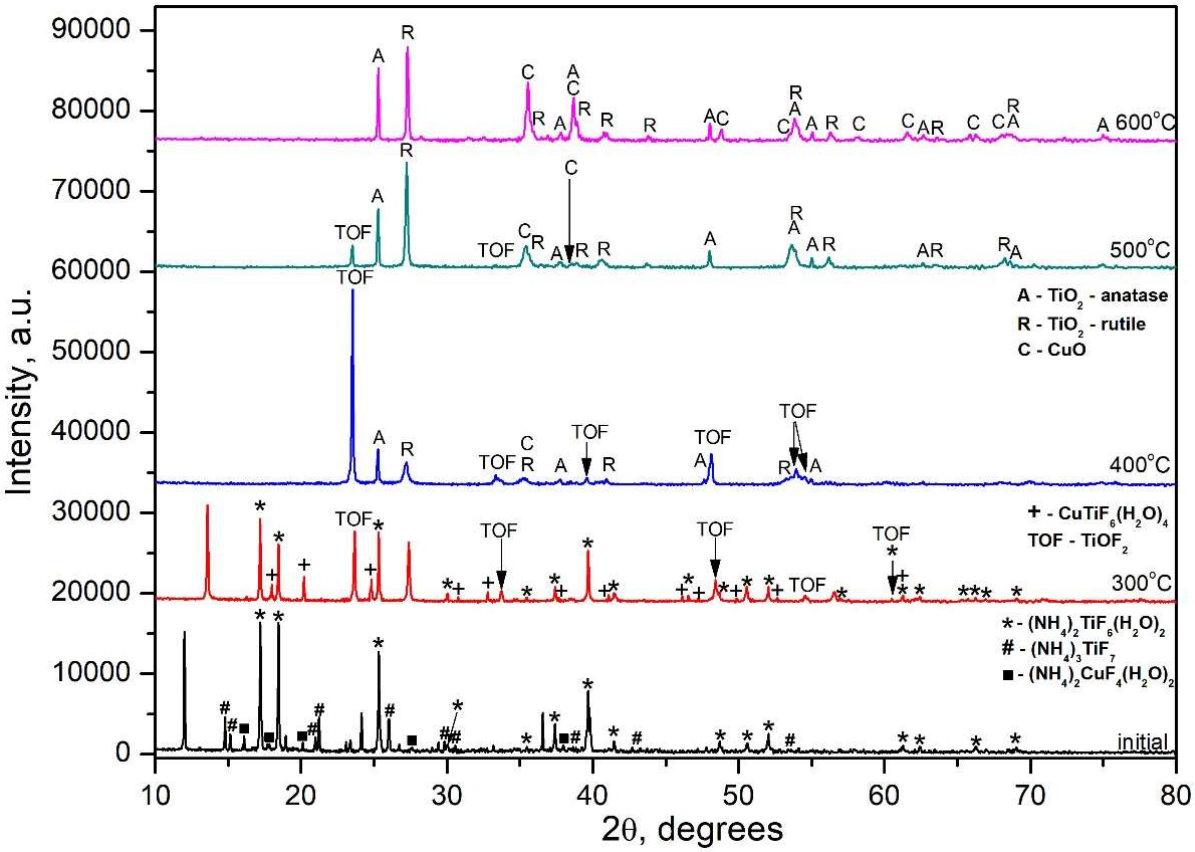

Figure 8. XRD diagrams of the samples with 10 wt.% of copper calculated in relation to CuO, precipitated at pH 6 and calcined for 1 hour at different temperatures.

Increased calcination temperature of 400 °C generated titanium dioxide formation in two phases, rutile and anatase, out of $TiOF_2$, as well as copper(II) oxide out of $CuTiF_6(H_2O)_4$. The phase composition was as follows:

- *h*-$TiOF_2$ – 39.3 wt.%,
- *c*-$TiOF_2$ – 20.6 wt.%,
- TiO_2 (anatase) – 13 wt.%,
- TiO_2 (rutile) – 18.7 wt.%,
- CuO – 8.4 wt.%.

There was also notable difference between the samples synthesized at pH 1 and the ones obtained at pH 6, after calcination at 400 °C. Namely, pH appeared to be a decisive factor in formation of TiO_2 phases. In the sample synthesized at pH 1, anatase prevailed in proportion 2:1. In contrast, pH 6 environment generated rutile domination in proportion 3:2.

Calcination at higher temperature of 500 °C had effect on the quantitative changes only. Here, the percentage of *h*-$TiOF_2$ was 5.5 wt.%, TiO_2 (anatase) – 16 wt.%, TiO_2 (rutile) – 69.2 wt.%,

and CuO – 12.4 wt.%. Qualitative composition remained unchanged. However, like in the case of the acid solution synthesis, the amount of the rutile phase of titanium dioxide remained larger than that of anatase. Thus, our assumption that copper ions added to the initial precursor would cause formation of titanium dioxide in two polymorphous structures, found its confirmation.

In the IR spectra of the particles synthesized at pH 6, shown in Fig. 9, the following absorption bands can be seen. The wide band with several maxima can be found between 3000 cm^{-1} and 3600 cm^{-1}, an intense absorption band with maximum at 1407 cm^{-1}, and absorption bands 984 cm^{-1} and 568 cm^{-1}. According to the available data (Nyquist and Kagel, 1971) these are typical for titanium tetrafluoride diammonium.

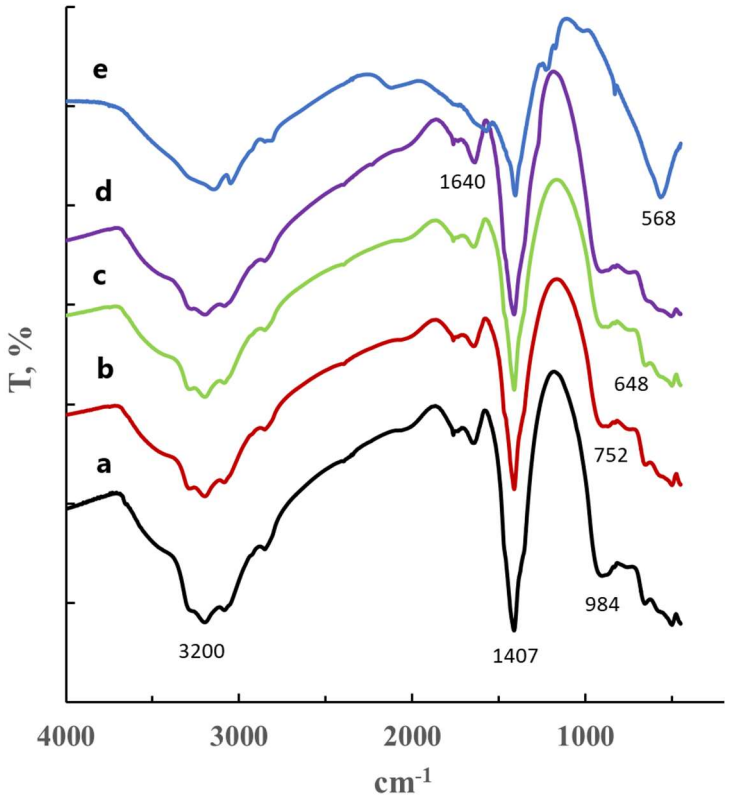

Figure 9. IR spectra of the particles synthesized at pH 6 with different proportion of copper (calculated in relation to CuO): a) 0.5 wt.%, b) 1 wt.%, c) 2 wt.%, d) 5 wt.%, and e) 10 wt.%.

The morphological features of the particles synthesized at pH 6 can be seen in Fig. 10. Unlike the ones synthesized at pH 1, these particles are formed in plate-like shapes of dimensions up to 5 μm and thickness of 0.4–0.6 μm (Figs. 10a–b). Increase of the copper proportion up to 10 wt.% caused differentiation of the particle forms, seen in Figs. 10c–d.

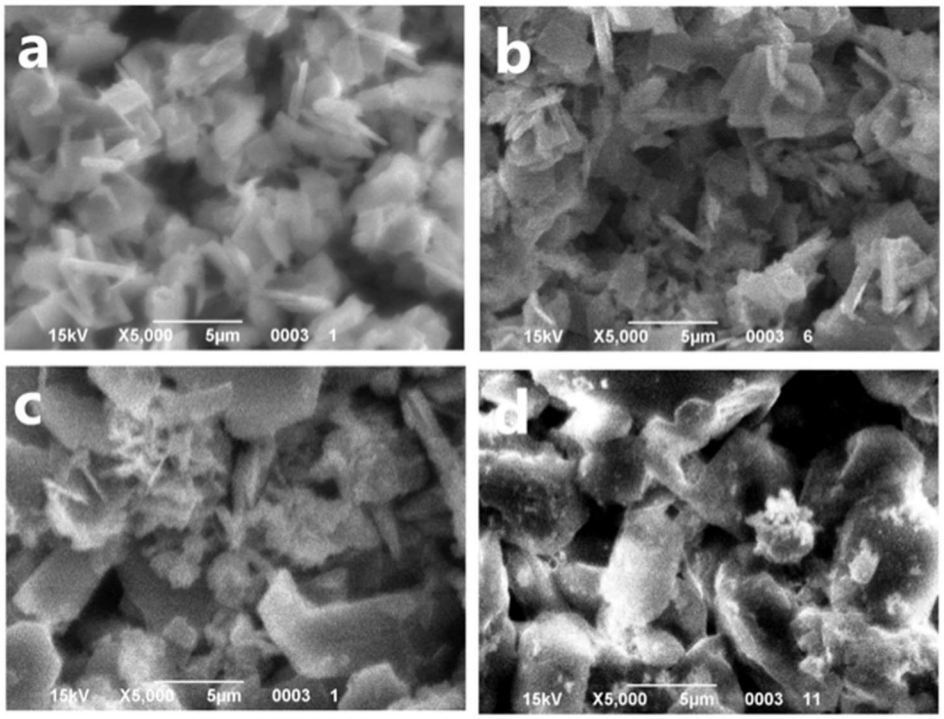

Figure 10. SEM images of the particles synthesized at pH 6 with different proportion of copper (calculated in relation to CuO): a) 0.5 wt.%, b) 1 wt.%, c) 5 wt.%, and d) 10 wt.%.

Results of XRD analysis correlated with the ones from analysis of IR spectra shown in Fig. 11. Thus, calcination at temperatures 300–500 °C caused decrease of intensity of absorption bands in the area between 3000 cm^{-1} and 3600 cm^{-1}, as well as of absorption band at 1428 cm^{-1}. In turn, after calcination at temperature 600 °C, the spectrum corresponded with titanium dioxide due to its typical wide absorption band in the area 1000–400 cm^{-1}. It should be noted that when copper content was higher than 5 wt.%, after calcination at 500 °C only one wide absorption band was observed between 1000 cm^{-1} and 500 cm^{-1}, typical for Ti–O bond in titanium dioxide. Hence, it can be stated that the addition of copper contributed to the titanium dioxide formation at lower temperatures.

SEM images of the particles synthesized with 1 wt.% of copper are shown in Fig. 12 It can be seen that for smaller copper concentrations during synthesis, below 2 wt.%, subsequent calcination temperature had no significant effect on the particle dimensions. However, for higher copper content of 10 wt.% some differences can be seen, dependent on calcination temperature. Figure 13 illustrates that at lower calcination temperatures of 300–500 °C the particle dimensions decreased. However, when the temperature was as high as 600 °C, large agglomerates were sintered up, with dimensions up to several micrometers.

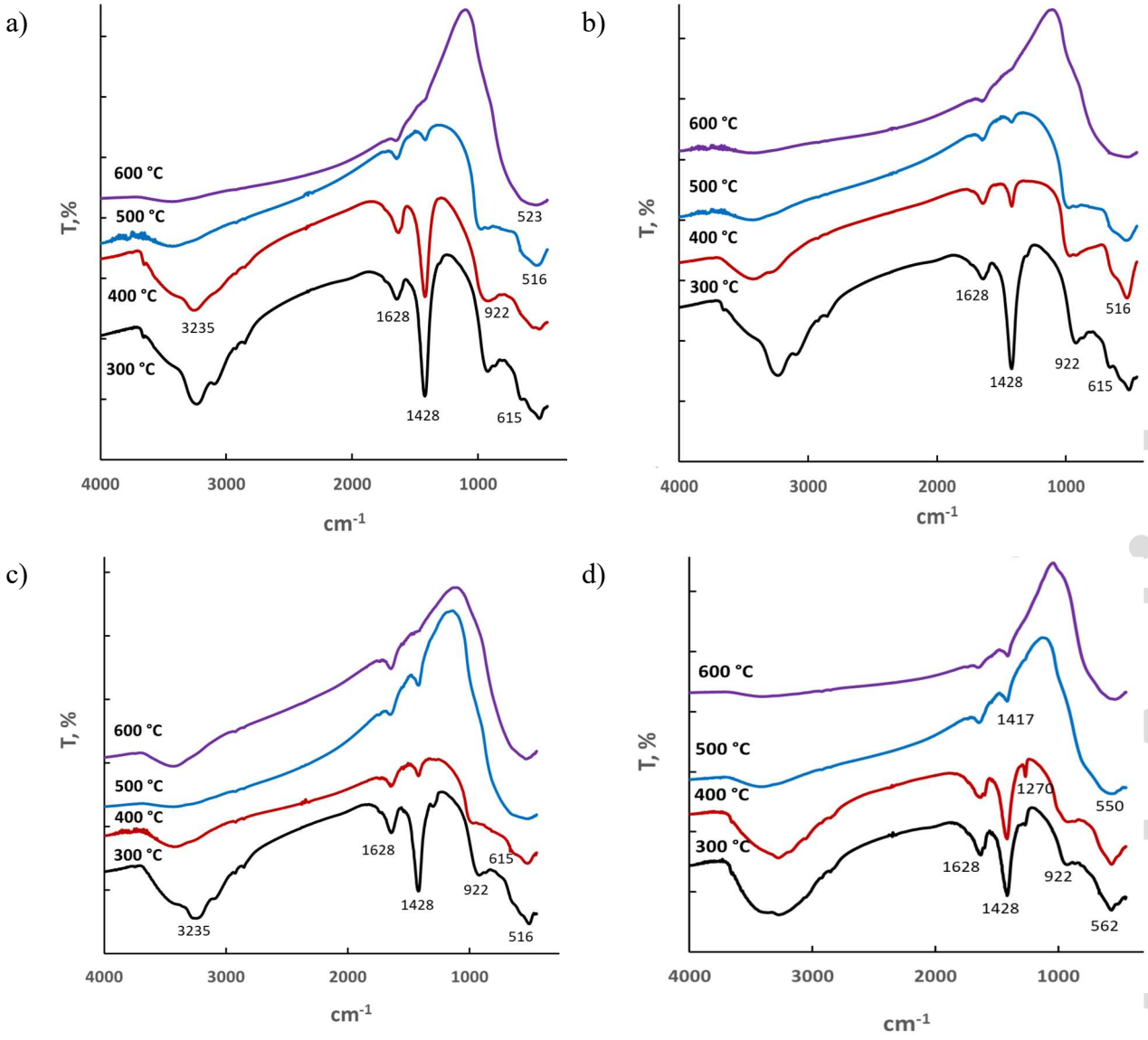

Figure 11. IR spectra of the particles synthesized at pH 6 and calcined at different temperatures for 1 hour, containing different proportion of copper (calculated in relation to CuO): a) 0.5 wt.%, b) 1 wt.%, c) 5 wt.%, and d) 10 wt.%.

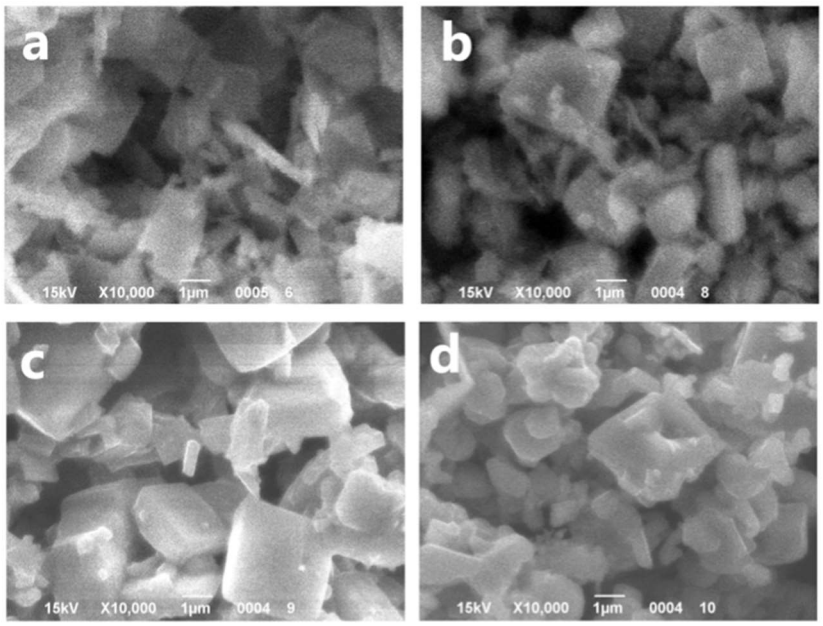

Figure 12. SEM images of the particles synthesized at pH 6 with 1 wt.% of copper calculated in relation to CuO, after calcination at different temperatures: a) 300 °C, b) 400 °C, c) 500 °C, d) 600 °C.

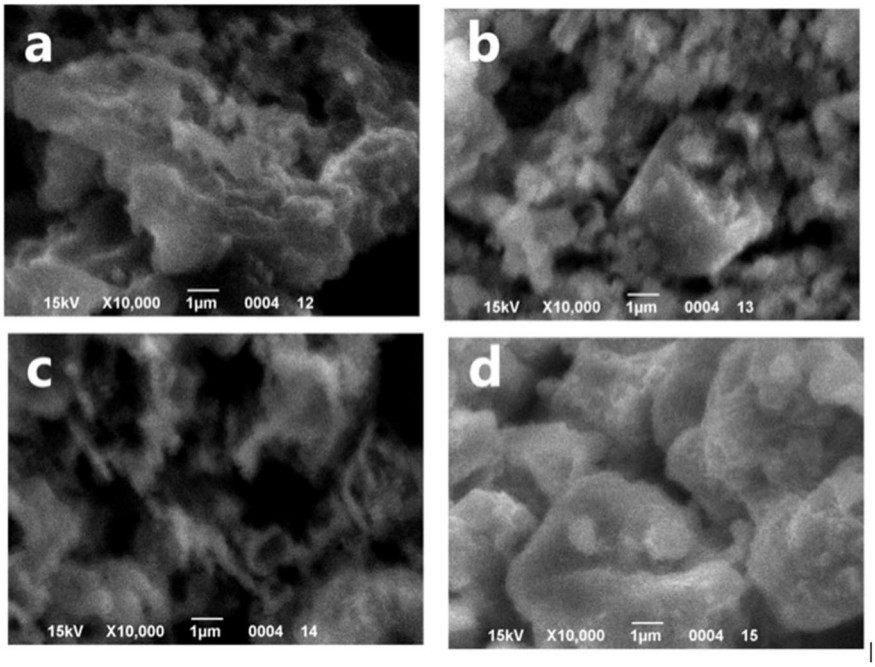

Figure 13. SEM images of the particles synthesized at pH 6 with 10 wt.% of copper calculated in relation to CuO, after calcination at different temperatures: a) 300 °C, b) 400 °C, c) 500 °C, d) 600 °C.

Results of the elemental analysis are collected in Table 4. It demonstrates that all the components $(NH_4)_2TiF_6(H_2O)_2$, $(NH_4)_3TiF_7$, and $(NH_4)_2CuF_4(H_2O)_2$ formed during synthesis underwent decomposition after calcination at temperatures above 300 °C. It is confirmed by the absence of nitrogen in the samples calcined at 400 °C.

Table 4. Elemental analysis results for the particles synthesized at pH 6.

Calcination temperature, °C	Element, wt.%				
	Ti	O	F	N	Cu
0.5 wt.% of CuO					
RT	26.3	11.5	52.3	9.7	0.2
300	28.1	13.3	50.5	7.9	0.2
400	33.7	12.0	51.8	2.1	0.4
500	41.7	20.1	37.7	-	0.5
600	51.3	45.3	2.8	-	0.6
1 wt.% of CuO					
RT	26.5	12.0	51.9	9.3	0.3
300	31.3	12.2	48.8	7.0	0.7
400	33.9	19.0	46.3	-	0.8
500	40.9	21.0	37.0	-	1.1
600	50.5	45.3	3.0	-	1.2
2 wt.% of CuO					
RT	25.5	12.0	52.2	9.6	0.7
300	31.0	12.2	50.2	5.0	1.6
400	31.9	19.0	47.0	-	2.1
500	40.4	21.0	35.7	-	2.9
600	50.0	43.3	3.6	-	3.1
5 wt.% of CuO					
RT	26.3	12.8	48.6	10.8	1.5
300	32.1	10.2	49.8	4.9	3.0
400	39.0	24.8	31.9	-	4.3
500	47.0	38.0	9.9	-	5.1
600	50.8	37.8	5.1	-	6.3
10 wt.% of CuO					
RT	20.6	7.6	50.0	11.1	5.0
300	21.1	12.0	57.0	5.0	3.1
400	36.1	23.6	35.0	-	5.3
500	36.0	34.0	22.4	-	7.6
600	47.2	37.0	6.5	-	9.3

However, decomposition of titanium oxyfluoride was observed at temperatures above 400°C, since significant decrease of fluorine content took place at temperatures 500 °C and higher. At the same time, in the samples calcined at 600 °C, presence of fluorine was still detectable, which indicated formation of fluorinated titanium dioxide F-TiO_2 (Dozzi et al., 2013; Shian

and Sandhage, 2010). It is worth noting that the fluorine content increased with the increase of copper concentration in the samples.

Thus, it was found that after precipitation out of neutral and alkaline solutions (at pH 6 and higher), the resulting powder consisted mainly of $(NH_4)_2TiF_6 \cdot 2H_2O$, $(NH_4)_3TiF_7$, and $(NH_4)_2CuF_4 \cdot 4H_2O$. Heating up to 300 °C caused decomposition of $(NH_4)_2CuF_4 \cdot 4H_2O$ with formation of $CuTiF_6 \cdot 2H_2O$. Also partial decomposition of $(NH_4)_2TiF_6 \cdot 2H_2O$ took place, as follows:

$$(NH_4)_2CuF_4 \rightarrow 2NH_3 + 2HF + CuF_2 \quad (3)$$

$$(NH_4)_2TiF_6 \rightarrow TiF_4 + 2NH_3 + 2HF \quad (4)$$

$$(NH4)_2TiF_6 + H_2O \rightarrow TiOF_2 + 2NH_3 + 4HF \quad (5)$$

$$CuF_2 + TiF_4 \rightarrow CuTiF_6 \quad (6)$$

When calcination temperature reached 400 °C, decomposition of $CuTiF_6$ took place with formation of copper(II) oxide and titanium oxyfluoride according to the reaction (1) above. Further increase of calcination temperature caused full decomposition of oxyfluoride with the formation of fluorinated titanium dioxide (rutile and anatase) according to the reaction (2).

3.3 Optical properties of the synthesized particles

Figure 14 presents diffuse reflectance spectra (DRS) of the particles synthesized at pH 1 and 6. Calculations proved that the increase of copper content caused slight decrease of the gap energies for the samples obtained in the acid solutions. In particular, for copper dopant content of 0.5 wt.% it was 3.3 eV, for 1 wt.% it was 2.25 eV, while for 5 wt.% it was 3.2 eV. In contrast, the opposite trend was observed for the samples synthesized in the alkaline solutions. Copper dopant content up to 5 wt.% did not cause significant changes of the absorption edge, but for 10 wt.% it shifted significantly toward ultraviolet area of the spectrum. At the same time, the band gap energy *Eg* increased up to 5.1 eV.

The calcination procedure had some effect on the diffuse reflectance spectra, as seen in Fig. 15. The absorption edge shifted somewhat toward visible spectrum area, which can be seen also from data provided in Table 5. At the same time, *Eg* decreased down to values of 3.05 eV and 3.14 eV for the particles synthesized at pH 1 and pH 6, respectively, and afterwards calcined at 600 °C.

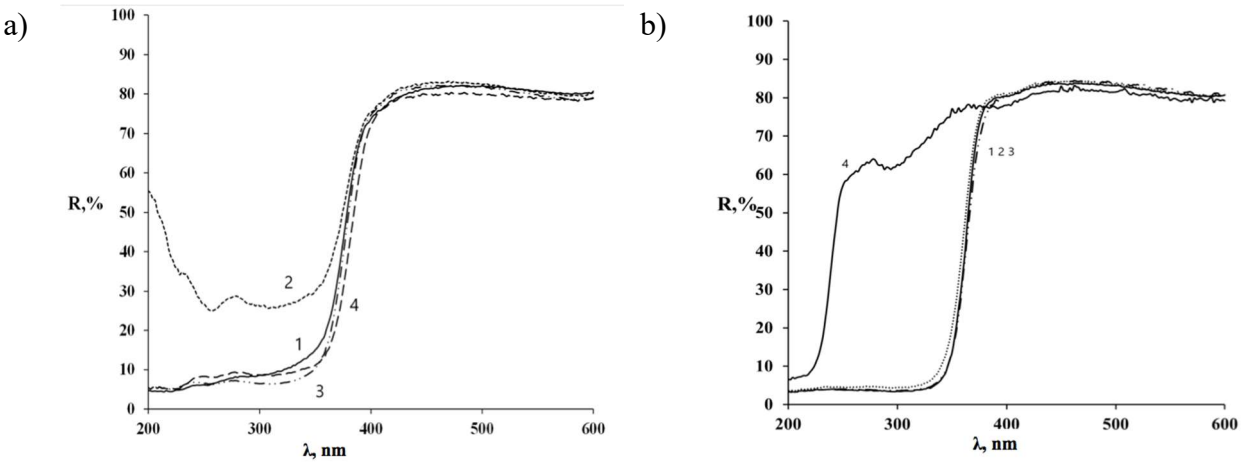

Figure 14. DRS UV–vis spectra of gap energies of the particles synthesized at pH 1 (a) and pH 6 (b) with respective copper content in the samples: 1 wt.% (curve 1), 2 wt.% (curve 2), 5 wt.% (curve 3), and 10 wt.% (curve 4), as calculated in relation to CuO.

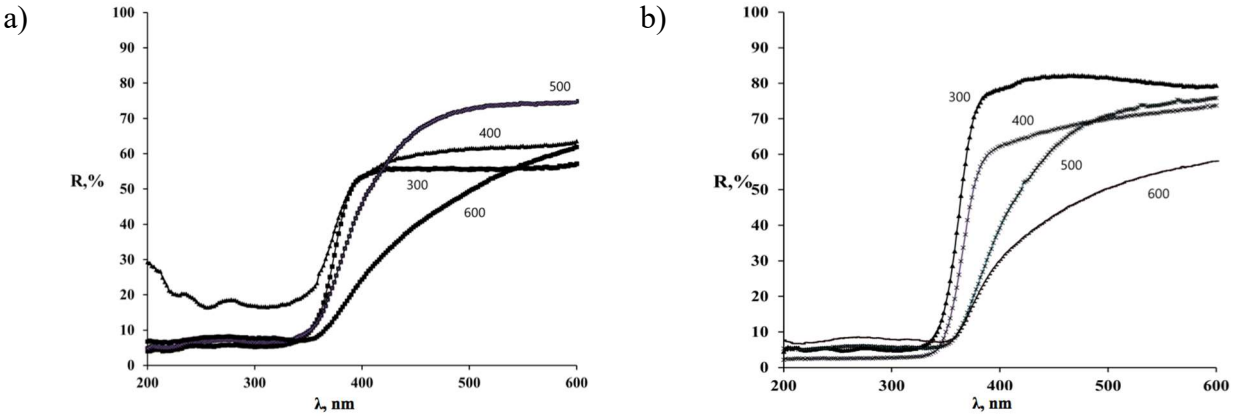

Figure 15. DRS UV–vis spectra of gap energies of the particles synthesized at pH 1 (a) and pH 6 (b) with copper content 5 wt.% calculated in relation to CuO, after calcination in air at different temperature for 1 hour.

The bandgap energy was estimated by plotting using Tauc's plot formula, $(\alpha h\nu)^{(1/2)}$ versus hν, where α is the absorption coefficient, and hν is the photon energy (eV) (Hajipour et al., 2021; Edelmannová et al., 2018). The example of band gap energy determination is shown schematically in Fig. 16.

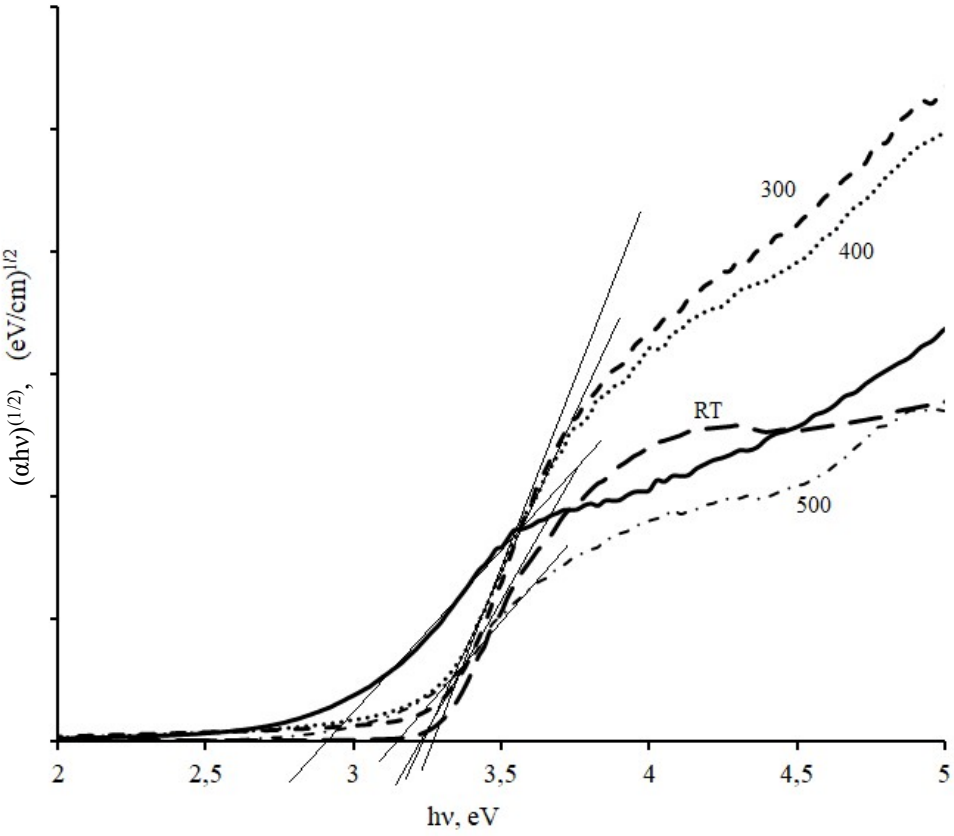

Figure 16. Band gap energy estimations from the plots of $(\alpha h\nu)^{(1/2)}$ versus hν for the particles synthesized at pH 1 with copper content 5 wt.% at different annealing temperatures.

In general, the results for F-TiO_2/CuO oscillated around the known characteristics of TiO_2, for anatase *Eg* = 3.2 eV, rutile *Eg* = 3.0 eV, and brookite *Eg* = 3.4 eV (Edelmannová et al., 2018). When CuO is present as a composite partner in CuO/TiO_2 nanocomposite, the band gap energy is shifted to lower energy (2.85-2.9 eV), indicating the visible light activity of the composite material. For instance, Baig et al. (2023) reported that addition of 30 wt.% of copper oxide CuO resulted with decrease of *Eg* down to 3.08 eV for the material CuO/TiO_2 obtained in the ultrasonic field, which increased its photocatalytic activity. In another paper (Hajipour et al., 2021) decrease of *Eg* down to 2.9 eV was demonstrated in TiO_2/CuO system after addition of CuO in proportion of 10 wt.%, which increased its antibacterial activity.

Table 5. Dependence of gap energies *Eg* on the calcination temperature for the samples synthesized at pH 1 and pH 6.

Copper dopant content, wt.%	Calcination temperature, °C	*Eg*, eV	
		pH=1	pH=6
0.5	-	3.25	3.40
	300	3.25	3.40
	400	3.25	3.35
	500	3.31	3.14
	600	3.08	3.20
1.0	-	3.25	3.42
	300	3.31	3.42
	400	3.31	3.35
	500	3.23	3.25
	600	3.15	3.17
2.0	-	3.18	3.50
	300	3.23	3.42
	400	3.28	3.40
	500	3.08	3.25
	600	3.00	3.20
5.0	-	3.23	3.40
	300	3.31	3.40
	400	3.25	3.28
	500	3.10	3.14
	600	2.90	3.12
10.0	-	3.33	5.14
	300	3.25	3.40
	400	3.18	3.35
	500	3.10	3.25
	600	2.85	2.90

So it is quite evident that the presence of CuO in the CuO/TiO_2 nanocomposites had a favorable effect on the light absorption characteristics, making it possible to exploit effectively the visible spectral region of the solar light. The increase of light absorption can contribute to the improvement of the photocatalytic properties.

4. CONCLUSIONS

The research results allow for formulating several important conclusions on the synthesis of F-TiO_2/CuO out of fluoride solutions and the effect of synthesis parameters on the structural features and properties of the obtained particles.

First of all, acid environment with pH<4 generated particles consisting of two structures of titanium oxyfluoride $TiOF_2$, cubic and hexagonal ones, as well as copper fluorotitanate tetrahydrate $CuTiF_6(H_2O)_4$. The latter underwent decomposition, fully completed at 400 °C. In turn, titanium oxyfluoride decomposition started at temperatures 300 – 400 °C and was completed at 600 °C with formation of titanium dioxide TiO_2 in rutile and anatase phases. Proportion of these two phases could be controlled by copper dopant concentration, since rutile content increased at higher Cu content. At the same time, increase of copper concentration caused full decomposition of titanium oxyfluoride at lower temperatures and increase of fluorine concentration in TiO_2.

In turn, neutral and alkaline solutions with pH>5 contributed to formation of the particles mainly consisting of $(NH_4)_2TiF_6 \cdot 2H_2O$, $(NH_4)_3TiF_7$, and $(NH_4)_2CuF_4 \cdot 4H_2O$. After calcination at temperature 300 °C, decomposition of $(NH_4)_2CuF_4 \cdot 4H_2O$ took place accompanied by formation of $CuTiF_6 \cdot 2H_2O$. Moreover, partial decomposition of $(NH_4)_2TiF_6 \cdot 2H_2O$ was observed. When the calcination temperature was increased up to 400 °C, $CuTiF_6$ underwent decomposition forming copper(II) oxide and titanium oxyfluoride. The latter would be fully decomposed at higher calcination temperatures with formation of fluorinated titanium dioxide F-TiO_2 , in rutile and anatase phases.

Another important finding was connected with photocatalytic properties, correlated with the band gap energy of the tested substances. The particles F-TiO_2/CuO synthesized at pH<4 exhibited *Eg* of 3.30–3.25 eV, which decreased down to 2.85 eV for higher copper concentrations (10 wt.% of CuO). Gap energy was slightly higher up to *Eg* 3.4–3.5 eV for F-TiO_2/CuO particles synthesized at pH>5, and it decreased down to 2.9 eV for higher copper concentrations.

Acknowledgement: This work was supported by the Ukrainian National Academy of Sciences, grant numbers 0122U200071, 0120U101777, and co-financed within the project PM/SP/0064/2021/1 titled "Intelligent measurement techniques in the diagnosis and forecasting of shaft cracks and their dimensional and shape accuracy", funded by the Ministry of Education and Science (Poland) as a part of the Polish Metrology Programme and co-financed within the project PM-II/SP/0040/2024/02 titled "A machine learning-aided

multisensor system for thermomechanical measurements and in-depth analysis of the surface layer in aircraft alloys", funded by the Ministry of Education and Science (Poland) as a part of the Polish Metrology Programme II.

REFERENCES

1. Abdalamir R.Q., Khodair Z.T., Abd A.N., 2022. Preparation and characterization of structural properties for TiO_2 and CuO nanostructures by sol-gel technique. *Materials Today: Proceedings*, 57, Part 2, 539–544. https://doi.org/10.1016/j.matpr.2022.01.417.
2. Amaral R., Blois C., Lunz J., Mello A., Jardim P., 2022. Physical and optical properties of Ag_3PO_4 decorated TiO_2 based nanostructures. *Journal of Solid State Chemistry*, 305, 122655. https://doi.org/10.1016/j.jssc.2021.122655.
3. Ayati A., Ahmadpour A., Bamoharram F.F., Tanhaei B., Mänttäri M., Sillanpää M., 2014. A review on catalytic applications of Au/TiO_2 nanoparticles in the removal of water pollutant. *Chemosphere*, 107, 163–174. https://doi.org/10.1016/j.chemosphere.2014.01.040.
4. Baig U., Dastageer M.A., Gondal M.A., Khalil A.B., 2023. Photocatalytic deactivation of sulphate reducing bacteria using visible light active CuO/TiO_2 nanocomposite photocatalysts synthesized by ultrasonic processing. *Journal of Photochemistry and Photobiology B: Biology*, 242, 112698. https://doi.org/10.1016/j.jphotobiol.2023.112698
5. Balaram V., Copia L., Kumar U.S., Miller J., Chidambaram S., 2023. Pollution of water resources and application of ICP-MS techniques for monitoring and management – A comprehensive review. *Geosystems and Geoenvironment*, 2/4, 100210. https://doi.org/10.1016/j.geogeo.2023.100210
6. Banas-Gac J., Radecka M., Czapla A., Kusior E., Zakrzewska K., 2023. Surface and interface properties of TiO_2/CuO thin film bilayers deposited by rf reactive magnetron sputtering. *Applied Surface Science*, 616, 156394. https://doi.org/10.1016/j.apsusc.2023.156394
7. Castañeda C., Martínez J.J., Santos L., Rojas H., Osman S.M., Gómez R., Luque R., 2022. Caffeine photocatalytic degradation using composites of NiO/TiO2–F and CuO/TiO2–F under UV irradiation. *Chemosphere*, 288/2, 132506. https://doi.org/10.1016/j.chemosphere.2021.132506
8. Chaudhari P., Mishra S., 2016. Effect of CuO as a dopant in TiO_2 on ammonia and hydrogen sulphide sensing at room temperature. *Measurement*, 90, 468–474. https://doi.org/10.1016/j.measurement.2016.05.007

9. Choudhury P., Ghosh B., Lamba O.P., Bist H.D., 1983. Phase transitions in $MnTiF_6 \cdot 6H_2O$ and $ZnTiF_6 \cdot 6H_2O$ observed by IR spectroscopy. *Journal of Physics C: Solid State Physics*, 16/9, 1609–1613. https://doi.org/10.1088/0022-3719/16/9/006
10. Chowdhury I.H., Ghosh S., Basak S., Naskar M.K., 2017. Mesoporous CuO-TiO_2 microspheres for efficient catalytic oxidation of CO and photodegradation of methylene blue. *J. Phys. Chem. Solids*, 104, 103–110. https://doi.org/10.1016/j.jpcs.2017.01.010
11. Cotolan N., Rak M., Bele M., Cör A., Muresan L.M., Milošev I., 2016. Sol-gel synthesis, characterization and properties of TiO_2 and Ag-TiO_2 coatings on titanium substrate. *Surface and Coatings Technology*, 307, Part A, 790–799. https://doi.org/10.1016/j.surfcoat.2016.09.082.
12. Cruz I.F., Freire C., Araújo J.P., Pereira C., Pereira A.M., 2018. Multifunctional Ferrite Nanoparticles: From Current Trends Toward the Future, In: El-Gendy A.A., Barandiarán J.M., Hadimani R.L. (Eds.), *Micro and Nano Technologies, Magnetic Nanostructured Materials*. Elsevier, Amsterdam, 59–116. https://doi.org/10.1016/B978-0-12-813904-2.00003-6
13. Dembski S., Schneider C., Christ B., Retter M., 2018. Core-shell nanoparticles and their use for in vitro and in vivo diagnostics, In: Focarete M.L., Tampieri A. (Eds.), *Core-Shell Nanostructures for Drug Delivery and Theranostics*. Woodhead Publishing, Duxford, 119–141. https://doi.org/10.1016/B978-0-08-102198-9.00005-3
14. Döbelin N., Kleeberg R., 2015. Profex: a graphical user interface for the Rietveld refinement program BGMN. *Journal of Applied Crystallography*, 48, 1573. doi.org/10.1107/S1600576715014685
15. Dozzi M.V., D'Andrea C., Ohtani B., Valentini G., Selli E., 2013. Fluorine-Doped TiO_2 Materials: Photocatalytic Activity vs Time-Resolved Photoluminescence. *The Journal of Physical Chemistry C*, 117/48, 25586–25595. https://doi.org/10.1021/jp4095563
16. Edelmannová M., Lin K.-Y., Wu J.C.S., Troppová I., Čapek L., Kočí K., 2018. Photocatalytic hydrogenation and reduction of CO_2 over CuO/TiO_2 photocatalysts. *Applied Surface Science*, 454, 313–318. https://doi.org/10.1016/j.apsusc.2018.05.123
17. Gao Y., Wang T., 2021. Preparation of Ag_2O/TiO_2 nanocomposites by two-step method and study of its degradation of RHB. *Journal of Molecular Structure*, 1224, 129049. https://doi.org/10.1016/j.molstruc.2020.129049
18. Garg A., Singhania T., Singh A., Sharma S., Rani S., Neogy A., Yadav S.R., Sangal V.K., Garg N., 2019. Photocatalytic Degradation of Bisphenol-A using N, Co codoped TiO_2 catalyst under solar light. *Sci. Rep.*, 9, 1–13. https://doi.org/10.1038/s41598-018-38358-w

19. Guo L., Zhang X., Meng F., Yuan J., Zeng Y., Han C., Jia Y., Gu M., Zhang S., Zhong Q., 2023. Synergistic effect of F and triggered oxygen vacancies over F-TiO2 on enhancing NO ozonation. *Journal of Environmental Sciences*, 125, 319–331. https://doi.org/10.1016/j.jes.2022.01.006
20. Gupta B., Melvin A.A., Matthews T., Dash S., Tyagi A.K., 2016. TiO_2 modification by gold (Au) for photocatalytic hydrogen (H_2) production. *Renewable and Sustainable Energy Reviews*, 58, 1366–1375. https://doi.org/10.1016/j.rser.2015.12.236.
21. Hajipour P., Eslami A., Bahrami A., Hosseini-Abari A., Saber F.Y., Mohammadi R., Mehr M.Y., 2021. Surface modification of TiO_2 nanoparticles with CuO for visible-light antibacterial applications and photocatalytic degradation of antibiotics. *Ceramics International*, 47/23, 33875–33885. https://doi.org/10.1016/j.ceramint.2021.08.300
22. Ibrahim N.S., Leaw W.L., Mohamad D., Alias S.H., Nur H., 2020. A critical review of metal-doped TiO_2 and its structure-physical properties – photocatalytic activity relationship in hydrogen production. *International Journal of Hydrogen Energy*, 45/53, 28553–28565. https://doi.org/10.1016/j.ijhydene.2020.07.233
23. Jacob K.A., Peter P.M., Jose P.E., Balakrishnan C.J., Thomas V.J., 2022. A simple method for the synthesis of anatase-rutile mixed phase TiO_2 using a convenient precursor and higher visible-light photocatalytic activity of Co–doped TiO_2. *Materials Today: Proceedings*, 49, Part 5, 1408–1417. https://doi.org/10.1016/j.matpr.2021.07.104.
24. Janczarek M., Klapiszewski Ł., Jędrzejczak P., Klapiszewska I., Ślosarczyk A., Jesionowski T., 2022. Progress of functionalized TiO_2-based nanomaterials in the construction industry: A comprehensive review. *Chemical Engineering Journal*, 430, 132062. https://doi.org/10.1016/j.cej.2021.132062
25. Kayani Z.N., Intizar T., Riaz S., Naseem S., 2021. Antibacterial, magnetic and dielectric properties of nano-structured V doped TiO_2 thin films deposited by dip coating technique. *Materials Chemistry and Physics*, 267, 124659. https://doi.org/10.1016/j.matchemphys.2021.124659.
26. Lathe A., Palve A.M., 2023. A review: Engineered nanomaterials for photoreduction of Cr(VI) to Cr(III). *Journal of Hazardous Materials Advances*, 12, 100333. https://doi.org/10.1016/j.hazadv.2023.100333
27. Li D., Haneda H., Hishita S., Ohashi N., Labhsetwar N.K., 2005. Fluorine-doped TiO_2 powders prepared by spray pyrolysis and their improved photocatalytic activity for decomposition of gas-phase acetaldehyde. *Journal of Fluorine Chemistry*, 126, 69–77. https://doi.org/10.1016/j.jfluchem.2004.10.044

28. Li F.-T., Liu R.-H., Zhao D.-S., Sun Z.-M., Qu Z.-M., 2007. Preparation and photocatalytic activity of nanoTiO2 codoped with fluorine and ferric. *Transactions of Nonferrous Metals Society of China*, 17, s713–s715.
29. Liang Z., Ouyang B., Wang T., Liu X., Huo H., Liu D., Feng H., Ma J., Deng K., Li A., Kan E., 2022. Pt modified TiO_2/NiO p-n junction with enhanced surface reaction and charge separation for efficient photocatalytic hydrogen evolution. *International Journal of Hydrogen Energy*, 47/20, 10868–10876. https://doi.org/10.1016/j.ijhydene.2022.01.140
30. Lin C.-J., Yang W.-T., 2014. Ordered mesostructured Cu-doped TiO_2 spheres as active visible-light-driven photocatalysts for degradation of paracetamol. *Chemical Engineering Journal*, 237/1, 131–137. https://doi.org/10.1016/j.cej.2013.10.027
31. Miklos D.B., Remy C., Jekel M., Linden K.G., Drewes J.E., Hübner U., 2018. Evaluation of advanced oxidation processes for water and wastewater treatment – A critical review. *Water Res*., 139, 118–131. https://doi.org/10.1016/j.watres.2018.03.042
32. Mittal A., Brajpuriya R., Gupta R., 2023. Solar steam generation using hybrid nanomaterials to address global environmental pollution and water shortage crisis. *Materials Today Sustainability*, 21, 100319. https://doi.org/10.1016/j.mtsust.2023.100319
33. Mohamed R.M., Kadi M.W., Ismail A.A., 2020. A Facile synthesis of mesoporous α-Fe_2O_3/TiO_2 nanocomposites for hydrogen evolution under visible light. *Ceramics International*, 46/10, Part A, 15604–15612. https://doi.org/10.1016/j.ceramint.2020.03.107.
34. Moridon S.N.F., Arifin K., Yunus R.M., Minggu L.J., Kassim M.B., 2022. Photocatalytic water splitting performance of TiO_2 sensitized by metal chalcogenides: A review. *Ceramics International*, 48/5, 5892–5907. https://doi.org/10.1016/j.ceramint.2021.11.199.
35. Núñez-Delgado A., Álvarez-Rodríguez E., Fernández-Sanjurjo M.J., Arias-Estévez M., Fernández-Calviño D., López-Ramón M.V., Sánchez-Polo M., 2023. Low-cost materials to face soil and water pollution. *Current Opinion in Environmental Science & Health*, 32, 100453. https://doi.org/10.1016/j.coesh.2023.100453
36. Nyquist R.A., Kagel R.O., 1971. *Infrared spectra of inorganic compounds*, Academic Press, New York and London.
37. Park H, Choi W., 2004. Effects of TiO_2 surface fluorination on photocatalytic reactions and photoelectrochemical behaviors. *Journal of Physical Chemistry B*, 108/13, 4086–4093. https://doi.org/10.1021/jp036735i
38. Poblete R., Cortes E., Salihoglu G., Salihoglu N.K., 2020. Ultrasound and heterogeneous photocatalysis for the treatment of vinasse from pisco production. *Ultrason. Sonochem*., 61, 104825. https://doi.org/10.1016/j.ultsonch.2019.104825

39. Riaz S., Park S.-J., 2020. An overview of TiO2-based photocatalytic membrane reactors for water and wastewater treatments. *Journal of Industrial and Engineering Chemistry*, 84, 23–41. https://doi.org/10.1016/j.jiec.2019.12.021
40. Rueda-Marquez J.J., Levchuk I., Ibañez P.F., Sillanpää M., 2020. A critical review on application of photocatalysis for toxicity reduction of real wastewaters. *J. Clean. Prod*., 258, 120694. https://doi.org/10.1016/j.jclepro.2020.120694
41. Shian S., Sandhage K.H., 2010. Hexagonal and cubic $TiOF_2$. *J. Appl. Crystallogr*., 43, 757–761. https://doi.org/10.1107/S0021889810016730
42. Siva Prasanna S.R.V., Balaji K., Pandey S., Rana S., 2019. Metal Oxide Based Nanomaterials and Their Polymer Nanocomposites, In: Karak N. (Ed.), *Nanomaterials and Polymer Nanocomposites*. Elsevier, Amsterdam, 123–144. https://doi.org/10.1016/B978-0-12-814615-6.00004-7
43. Sofronov D., Rucki M., Doroshenko A., Shaposhnyk A., Kapustnik O., Mateychenko P., Baumer V., Zurowski W., 2022. Synthesis of TiO_2 nanoparticles out of fluoride solutions. *Journal of Materials Research and Technology*, 17, 2267–2279. https://doi.org/10.1016/j.jmrt.2022.02.002.
44. Sofronov D.S., Lebedynskiy O.M., Rucki M., Mateychenko P.V., Minenko S.S., Shaposhnyk A.M., Krzysiak Z., 2023. A novel method of $TiOF_2$ particles synthesis out of fluoride solutions. *Journal of Alloys and Compounds*, 966, 171646. https://doi.org/10.1016/j.jallcom.2023.171646.
45. Szczepanik B., 2017. Photocatalytic degradation of organic contaminants over clay-TiO_2 nanocomposites: A review. *Applied Clay Science*, 141, 227–239. https://doi.org/10.1016/j.clay.2017.02.029
46. Tatarchuk T., Peter A., Al-Najar B., Vijaya J., Bououdina M., 2018. Photocatalysis: Activity of Nanomaterials, In: Hussain C.M., Mishra A.K. (Eds.), *Nanotechnology in Environmental Science*. Wiley-VCH Verlag GmbH & Co. KGaA, Weinheim, 209–292. https://doi.org/10.1002/9783527808854.ch8
47. Todorova N., Giannakopoulou T., Romanos G., Vaimakis T., Yu J., Trapalis C., 2008. Preparation of fluorine-doped TiO_2 photocatalysts with controlled crystalline structure. *International Journal of Photoenergy*, 2008, 534038. https://doi.org/10.1155/2008/534038
48. Wang J., Cao F., Bian Z., Leung M.K., Li H., 2014. Ultrafine single-crystal $TiOF_2$ nanocubes with mesoporous structure, high activity and durability in visible light driven photocatalysis. *Nanoscale*, 2, 897–902. https://doi.org/10.1039/C3NR04489K

49. Wang X., Li S., Chen P., Li F., Hu X., Hua T., 2022. Photocatalytic and antifouling properties of TiO_2-based photocatalytic membranes. *Materials Today Chemistry*, 23, 100650. https://doi.org/10.1016/j.mtchem.2021.100650
50. Wang Y., Gao P., Li B., Yin Z., Feng L., Liu Y., Du Z., Zhang L., 2022. Enhanced photocatalytic performance of visible-light-driven CuO_x/TiO_{2-x} for degradation of gaseous formaldehyde: Roles of oxygen vacancies and nano copper oxides. *Chemosphere*, 291/1, 133007. https://doi.org/10.1016/j.chemosphere.2021.133007